Monthly Notices
of the
ROYAL ASTRONOMICAL SOCIETY

MNRAS **486,** 3685–3696 (2019)
Advance Access publication 2019 April 17

doi:10.1093/mnras/stz1099

Launching of hot gas outflow by disc-wide supernova explosions

Evgenii O. Vasiliev,[1,2,3]★ Yuri A. Shchekinov[3,4]★ and Biman B. Nath[4]★

[1]*Southern Federal University, Stachki Ave. 194, Rostov-on-Don 344090, Russia*
[2]*Special Astrophysical Observatory, Russian Academy of Sciences, Nizhnii Arkhyz, Karachaevo-Cherkesskaya Republic 369167, Russia*
[3]*Lebedev Physical Institute of Russian Academy of Sciences, 53 Leninskiy Ave., Moscow 119991, Russia*
[4]*Raman Research Institute, Sadashiva Nagar, Bangalore 560080, India*

Accepted 2019 April 15. Received 2019 March 21; in original form 2019 January 3

ABSTRACT

Galactic gas outflows are driven by stellar feedback with dominant contribution from supernova (SN) explosions. The question of whether the energy deposited by SNe initiates a large-scale outflow or gas circulation on smaller scales – between discs and intermediate haloes – depends on SN rate and their distribution in space and time. We consider here gas circulation by disc-wide unclustered SNe with galactic star formation rate (SFR) in the range from $\simeq 6 \times 10^{-4}$ to $\simeq 6 \times 10^{-2}$ $M_\odot$ yr^{-1} kpc^{-2}, corresponding to mid-to-high star formation (SF) observed in galaxies. We show that such disc-wide SN explosion regime can form circulation of warm ($T \sim 10^4$ K) and cold ($T < 10^3$ K) phases within a few gas scale heights, and elevation of hot ($T > 10^5$ K) gas at higher ($z > 1$ kpc) heights. We found that the threshold energy input rate for hot gas outflows with disc-wide SN explosions is estimated to be of the order $\sim 4 \times 10^{-4}$ erg s^{-1} cm^{-2}. We discuss the observational manifestations of such phenomena in optical and X-ray bands. In particular, we found that for face-on galaxies with SF ($\Sigma_{\rm SF} > 0.02\,M_\odot$ yr^{-1} kpc^{-2}), the line profiles of ions typical for warm gas show a double-peak shape, corresponding to out-of-plane outflows. In the X-ray bands, galaxies with high SFRs ($\Sigma_{\rm SF} > 0.006\,M_\odot$ yr^{-1} kpc^{-2}) can be bright, with a smooth surface brightness in low-energy bands (0.1–0.3 keV) and patchy at higher energies (1.6–8.3 keV).

Key words: shock waves – ISM: bubbles – galaxies: ISM.

1 INTRODUCTION

Supernova (SN) explosions are thought to be the principal energy source for supplying heavy elements (metals) into galactic haloes and circumgalactic gas by means of gaseous outflows perpendicular to galactic discs (Suchkov et al. 1994; Mac-Low & Ferrara 1999; Vijayan et al. 2018). Two different scenarios are usually considered: (i) the first suggests a starburst followed by multiple SN explosions in galactic centre, and (ii) the second is connected with star formation (SF) in isolated OB-associations spread throughout the disc. The second is apparently more efficient in the sense that for a given total mechanical luminosity the amount of hot (X-ray) gas above the plane is larger (see for recent discussion in Vijayan et al. 2018). The differences between these scenarios, their observational manifestations, and large-scale feedback have been widely debated since Thompson, Quataert & Norman (2005), for more recent discussion see Rubin et al. (2014), Wibking, Thompson & Krumholz (2018), Girichidis, Walch & Naab (2016), Gatto et al. (2017), Fielding et al. (2017), Fielding, Quataert & Martizzi (2018).

In the discussion of mass transport by SF activity, an issue of primary importance is the critical star formation rate (SFR) able to produce sufficient amount of energy for elevating mass from discs into haloes. In terms of the surface energy injection rate observational estimates for strong galactic winds driven by a central starburst, the injection threshold rate has been estimated as $\epsilon \sim 10^{-2}$ erg cm^{-2} s^{-1} (Lehnert & Heckman 1996; Heckman 2002, 2003), while for disc-wide case the estimates are an order of magnitude lower 10^{-3} erg cm^{-2} s^{-1} as inferred from synchrotron (Dahlem, Liesenfeld & Golla 1995; Dahlem, Liesenfeld & Rossa 2000) and from X-ray and far-infrared emission (Tüllmann et al. 2006) of the haloes of edge-on galaxies. However, galactic winds do exist at a much lower energy injection rate: Li & Wang (2013) have reported observation of an X-ray bright galactic corona with underlying SFR equivalent to only $\epsilon \sim 10^{-5}$ erg cm^{-2} s^{-1} at the lower end. More recently, Rubin et al. (2014) based on the analysis of 105 galaxies in the local Universe ($0.3 < z < 1.4$) claimed 'no evidence for a threshold' of the injection rate.

One can think that the threshold energy rate can vary depending on deposition rate of energy from SF and the regime in which this energy is deposited – namely, whether SF occurs mostly in large

★ E-mail: eugstar@mail.ru (EOV); yus@asc.rssi.ru (YAS); biman@rri.res.in (BBN)

stellar clusters or in smaller clusters with only a few O-stars – SN progenitors. In first case with large stellar clusters SN explosions can drive large scale outflows, in the second their feedback can maintain only circulation of gas within a few vertical scales. Observationally the former can give rise to such events as a powerful wind in M82, while the latter can reveal as a 'boiling' galaxy NGC 253 (Sofue, Wakamatsu & Malin 1994) and massive intermediate haloes in edge-on galaxies like NGC 891 (Rossa et al. 2004). We focus here on the latter case with disc-wide unclustered SN explosions.

Therefore, the lower limit of the energy injection rate – if it exists, and physical processes that can cause this limit are of great importance for understanding global circulation of matter and heavy elements in the Universe.

Currently most of the numerical experiments in driving disc-to-haloes outflows are based on the galactic wind model with continuous energy injection into a fixed volume, as described in the seminal paper by Chevalier & Clegg (1985). Essentially it suggests that the energy injection rate is $\dot{E} \sim \nu_{\rm sn} E_{\rm sn}$, with $\nu_{\rm sn}$ ($\rm s^{-1}$) and $E_{\rm sn}$ being the rate of SN explosions in a given (injection) volume and the explosion energy, correspondingly. This assumption has been substantiated numerically in a spherically symmetric model for a uniform medium in (Sharma et al. 2014): for a sufficiently high SN rate in a given volume hydrodynamic fields (velocity, density, pressure radial profiles) and the integral behaviour converge to the analytic self-similar solution described in (Chevalier & Clegg 1985). Moreover, in this limit the heating efficiency – the fraction of SN energy converted into thermal and kinetic energy of the expanding (super)bubble, increases and asymptotically tends to $\eta_{\rm h} \simeq 0.4$ weakly depending on ambient density n (Sharma et al. 2014; Vasiliev et al. 2015). For a low SN rate – $\nu_{\rm sn} < 10^{-12}$ $\rm yr^{-1}$ $\rm pc^{-3}$, the efficiency falls down $\eta_{\rm h} < 0.08$, with a scaling $\eta_{\rm sh} \propto \nu_{\rm sn}^{0.2} n^{-0.6}$ (Vasiliev et al. 2015). At such conditions, the launch and dynamics of outflows driven by stellar feedback can be described numerically in the luminosity driven mode with continuous mechanical luminosity $L \approx \nu_{\rm sn} \eta_{\rm h} E_{\rm sn}$.

However, this conclusion changes for SN explosions in a vertically stratified interstellar medium (ISM). In this case after a few SN explosions the growing bubble can break through the disc and form a cavity growing upwards, and all subsequent explosions expand in a very low density bubble interior with a minimum energy loss with $\eta_{\rm h} \sim 0.6$ (Fielding et al. 2018; Shchekinov 2018). This means that an adequate description of outflows should involve injection of energy from individual SN explosions. Moreover, the approach based on a continuous luminosity driven model is inherently an average description, i.e. $L = \nu_{\rm sn} E_{\rm sn} = E_{\rm sn} \langle \sum_i \delta(t - t_i) \delta(\boldsymbol{r} - \boldsymbol{r}_i) \rangle$, where t_i and $\boldsymbol{r}_i$ is the time and the position of an i-th SN explosion. As such it may miss dynamical and morphological details connected with a random character of explosions. For separate individual explosions mechanical luminosity is a random function $L(t, \boldsymbol{r}) = E \sum_i \delta(t - t_i) \delta(\boldsymbol{r} - \boldsymbol{r}_i)$, and its dynamical feedback depends on particular configuration of the sets $[t_i]$ and $[\boldsymbol{r}_i]$ and their statistical properties, such as characteristic separation between in the set of t_i and in the set of $\boldsymbol{r}_i$.

The issue of mass transport by individual SNe spread randomly in stellar discs has been address in several previous studies, including Kim & Ostriker (2018). However, the question we address in this paper is not only the efficiency of such energy injection, but the possible observational manifestations, and the observational diagnostics that can tell us about the mass transport rate. The paper is organized as follows. Section 2 contains model description and numerical set-up, in Section 3 we describe the results, while in Section 4 we discuss observational manifestations, details of the model, Section 5 summarizes the results.

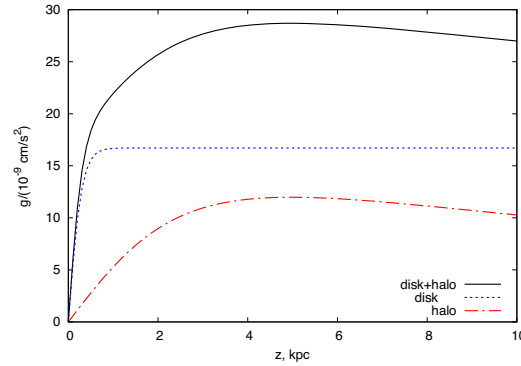

Figure 1. Gravitational acceleration versus height z at the cylindrical radius 3 kpc as defined by equation (1) for the model $\Sigma_{\rm g} = 3.6$ $\rm M_\odot$ $\rm pc^{-2}$. Dotted and dot–dashed lines show contributions from the stellar disc and from the halo, their sum is shown by solid line.

2 MODEL DESCRIPTION AND NUMERICAL SET-UP

We carry out 3D hydrodynamic simulations (Cartesian geometry) of multiple SN explosions in the galactic disc. We set up a gaseous disc to be initially in the hydrostatic equilibrium in a gravitational potential (as in many previous papers, see e.g. de Avillez 2000; Hill et al. 2012; Walch et al. 2015; Li, Bryan & Ostriker 2017a), which consists of two components: a dark matter (DM) halo and a baryonic disc. In cylindrical coordinates with z-axis perpendicular to the disc, the z-component of the gravitational acceleration due to the DM halo is calculated from a Navarro–Frenk–White profile: $g_{\rm DM}(z) = GM_{\rm DM}(r)z/r^3$, where $M_{\rm DM}$ is the DM mass enclosed within radius r and we adopt virial radius of the halo equal to 200 kpc and concentration parameter $c = 12$.

The baryonic disc is assumed to be self-gravitating with an isothermal velocity dispersion. The acceleration perpendicular to the disc is $g_*(z) = 2\pi G \Sigma_* \tanh(z/z_*)$, where Σ_* and z_* are the stellar surface density and scale height of the stellar disc, respectively. Contribution from a gaseous disc is included, following Li et al. (2017a), by dividing $g_*(z)$ by $f_* = \Sigma_*/(\Sigma_* + \Sigma_{\rm gas})$, that implicitly suggests the gaseous disc to be non-self-gravitating. Thus, the z-component of the total gravitational acceleration is calculated as (Li et al. 2017a)

$$g(z) = GM_{\rm DM}(r)\frac{z}{r^3} + \frac{1}{f_*} 2\pi G \Sigma_* \tanh\left(\frac{z}{z_*}\right). \quad (1)$$

Fig. 1 shows $g(z)$ within the heights of interest at the cylindrical radial distance $R = 3$ kpc, for which the value of z_* is assumed to be equal 0.3 kpc as it has been estimated in the solar neighbourhood (Gilmore & Reid 1983), the stellar surface density equals to $\Sigma_* =$ 180 $\rm M_\odot$ $\rm pc^{-2}$ and gas surface density $\Sigma_{\rm g} = 3.6$ $\rm M_\odot$ $\rm pc^{-2}$. The contributions from the stellar component and from the halo are shown by dotted and dot–dashed lines. Similar model for the potential gradient has been used for simulations of multiphase galactic outflows (e.g. Li et al. 2017a), and is consistent with the model of gravitational potential built by Kalberla (2003) at the cylindrical radial distance 3 kpc from the Milky Way centre (see fig. 7 in Kalberla 2003). It is adopted as a fiducial case in our simulations, unless otherwise specified.

In our models we consider two values for gas surface density: $\Sigma_g = 3.6$ and 10.8 $M_\odot$ pc^{-2}. The first value Σ_g is considered here as fiducial. The second value of gas surface density is very close to the observed density in the Milky Way disc at the Solar circle (see in Kalberla 2003; Kalberla & Kerp 2009), and the one considered in section 4.3 of Li et al. (2017a); the mid-plane number density in these models are 1 and 3 cm^{-3}, respectively.

The gas density profile is found from the hydrostatic equilibrium. At large heights the number density is kept uniform at 10^{-3} cm^{-3}. The gas surface density $\Sigma_g = 3.6$ $M_\odot$ pc^{-2} corresponds to the number density at the mid-plane 1 cm^{-3}. Initially the gas temperature is 9×10^3 K; the gas metallicity is kept constant equal to the solar value within the entire computational domain. Standard simulations are performed with a physical cell size of 2 pc in the computational domain with $256 \times 256 \times 768$ cells, that corresponds to $512 \times 512 \times 1536$ pc^3. Note that in the case of high SN rate a significant part of gas from the disc may leave our standard computational box. In this case we expand the box from 1.5 to 16 kpc, and increase the physical cell size to 4 pc. We ensured that this increase does not affect the evolution of the physical parameters considered here, e.g. velocity distribution, mass fraction, emission characteristics.

SNe are distributed randomly and uniformly in the galactic plane and exponentially in the vertical direction. The scale height is 1/3 of the stellar scale height, i.e. $h_{SN} = 0.1$ kpc – it is consistent with the scale height of the youngest star-forming disc in the Milky Way (Hakobyan et al. 2017), see also discussion in Walch et al. (2015) and Li et al. (2017a). SN events follow one-after-one uniformly in time; we ran models with the averaged time delay Δt from 10^6 to 10^4 yr. Using the sizes of the computational domain and SN scale height, one can easily find the volume (ν_{SN}) and surface (Σ_{SN}) SN rates. Thus, the volume SN rate ν_{SN} ranges from 2×10^{-14} to 2×10^{-12} yr^{-1} pc^{-3}. The surface density of SFR corresponding to the volume SN rate equals $\Sigma_{SF} = 2 h_{SN} \nu_{SN} m_0$, where $m_0 = 150$ $M_\odot$ for a Salpeter IMF, or in the normalized form

$$\Sigma_{SF} \simeq 5.7 \times 10^{-2} M_\odot \mathrm{yr}^{-1}\ \mathrm{kpc}^{-2} \left(\frac{h_{SN}}{0.1\ \mathrm{kpc}}\right) \times \left(\frac{\nu}{2 \times 10^{-12} \mathrm{yr}^{-1} \mathrm{pc}^{-3}}\right). \quad (2)$$

One should stress here that we do not fit directly the adopted SN (and correspondingly SF) rates to the Kennicutt–Schmidt (KS) law. Indeed, to the highest SN rate considered here the Σ_{SFR} value should correspond to the range of gas surface density $\sim$10$-$100 $M_\odot$ pc^{-2} in the KS relation (Schmidt 1959; Kennicutt 1998) and is obviously much higher than that adopted in our simulations. Although our focus here is a particular aspect of stellar feedback – gas circulation in galactic discs, it is worth noting that the KS relation in the high surface density end is inferred from measurements of H α, H I, far-infrared continuum, and CO emissions averaged over a relatively low angular resolution (see discussion in Kennicutt 1998; Bigiel et al. 2008). As such it can be applicable only to large areas of galactic discs. At sub-kpc scales it may not be valid because star-forming molecular clouds are quickly (within a few Myr to tens of Myr) destroyed by feedback from massive stars, and the SNe explode mostly in regions of lower density [see for discussion of observational aspects in Kennicutt & Evans (2012), and theoretical arguments in Krumholtz, Dekel & McKee (2012), Khoperskov & Vasiliev (2017), and Semenov, Kravtsov & Gnedin (2018)]. From this point of view our models illustrate transport of mass from the regions of galactic discs cleaned from dense molecular gas by stellar feedback. It is obvious that SN-driven ejection of denser molecular gas from discs with higher Σ_g is less efficient.

It is also worth emphasizing that individual SNe are assumed here to be immersed in a smooth interstellar environment with the density distribution corresponding to an average density without considering effects from a parent molecular cloud. Such a description is common when large-scale effects in SN-driven ISM are concerned (see discussion in Vasiliev et al. 2015, 2017; Li et al. 2017a; Li, Bryan & Ostriker 2017b; Fielding, Quataert & Martizzi 2018; Vijayan et al. 2018; Melso, Bryan & Li 2019, and references therein). On the contrary, study of many issues connected with 'microscopic' scales of SN ejecta interaction with dense molecular environment in the parent molecular clouds, in particular, with generation of cosmic rays in superbubbles, do concern dynamics of an SN shock propagating in an immediate surrounding dense molecular material (see review in Frisch & Dwarkadas 2018). In this latter case, only a fraction (still rather uncertain) of SN energy is deposited into ISM on large scales comparable to the scale height of gas. Therefore, the numerical values of SN rates assumed in numerical simulations of stellar feedback on large galactic scales has to be increased by an uncertain factor $f \sim 1$ in order to account SN explosions hidden in their parent molecular clouds.

Location of the SN explosions does not correlate the gas density. In all models SN rate does not change with time; this is equivalent to a constant SFR. The random times and locations of SNe are chosen at initialization, such that for all runs with a given configuration, SNe explode in the same locations. Note that for very low SN rates remnants of individual SNe can cool down separately before they merge into a collective bubble. We restrict our simulations within a time-scale of a single starburst $\lesssim 30$ Myr. We inject the mass ($10\,M_\odot$) and energy (10^{51} erg) of each SN in a region of radius $r_0 =$ 3 pc (4 pc for the grid with the resolution 4 pc), with the energy injected as thermal energy. It is worth stressing here that the cooling radius for an expected gas temperature behind the shock fronts $T \sim 10^5$–10^7 K is $\ell_{cool} \gtrsim 10^{20} n_0^{-1}$ cm is considerably (at least factor of 7) larger than the injection r_0. Kim & Ostriker (2015) showed that $\ell_{cool}/r_0 \geq 3$ is sufficient for the Sedov–Taylor phase to settle on consistently. We compared the evolution of a bubble formed by an isolated SN with the current spatial resolution with several high-resolution simulations (0.15 pc, see appendix A in Vasiliev et al. 2017), and found the current resolution to describe overall evolution consistently with the correct time for the to settle on to the Sedov–Taylor phase; a brief discussion of possible sub-grid effects related to radiation losses can be found in Sharma et al. (2014).

The code is based on the unsplit total variation diminishing approach that provides high-resolution capturing of shocks and prevents unphysical oscillations. We have implemented the Monotonic Upstream-Centred Scheme for Conservation Laws (MUSCL)-Hancock scheme and the Haarten–Lax–van Leer-Contact (HLLC) method (see e.g. Toro 1999) as an approximate Riemann solver. This code has successfully passed the whole set of tests proposed in Klingenberg, Schmidt & Waagan (2007).

Simulations are run with radiative cooling processes with a tabulated non-equilibrium cooling function fitting the calculated one (Vasiliev 2011, 2013). The fitted function is obtained for gas cooling isochorically from 10^8 K down to 10 K. The non-equilibrium calculation (Vasiliev 2011, 2013) includes kinetics of all ionization states of H, He, C, N, O, Ne, Mg, Si, Fe, as well as kinetics of molecular hydrogen at $T < 10^4$ K.

We apply a diffuse heating term representing the photoelectric heating of dust grains (Bakes & Tielens 1994), which is thought to be the dominant heating mechanism in the interstellar medium. In

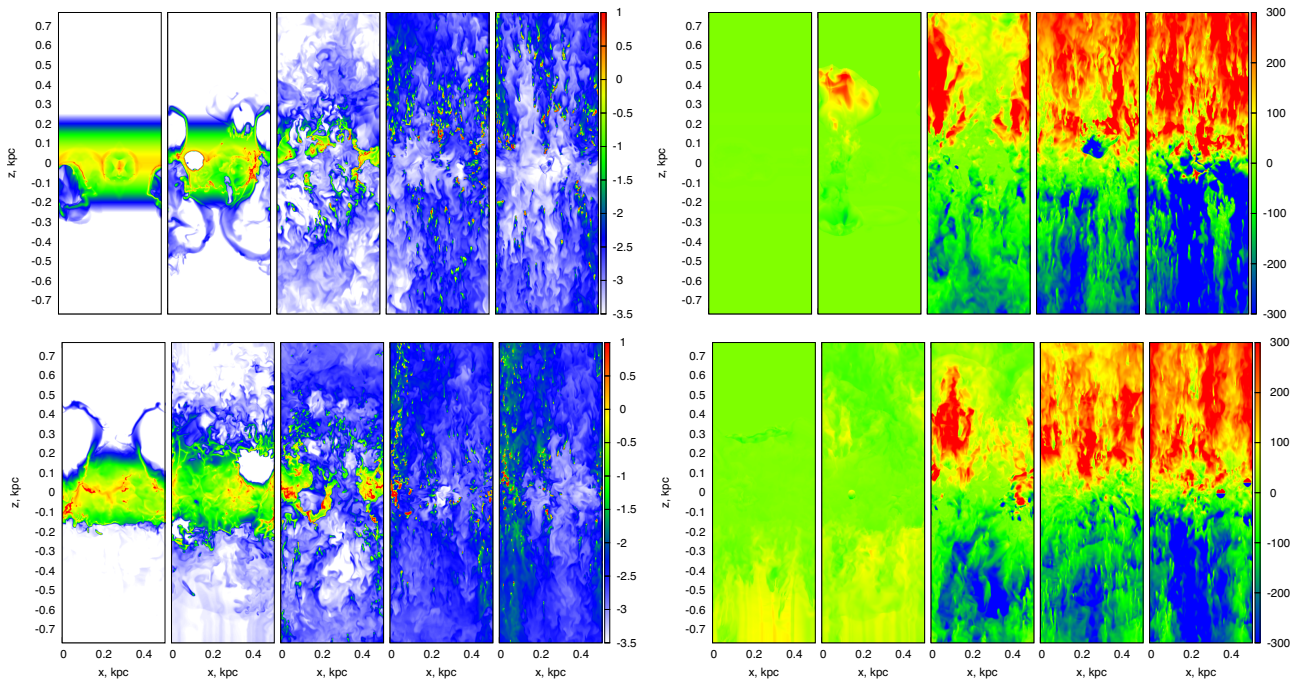

Figure 2. 2D slices showing gas number density [$\log(n, \mathrm{cm}^{-3})$, left-hand panels] and velocity in z-direction (v in km s^{-1}, right-hand panels) distribution in outflows for different SN rate in the disc with gas surface density $\Sigma_\mathrm{g} = 3.6\ \mathrm{M}_\odot\ \mathrm{pc}^{-2}$: 2×10^{-14}, 6×10^{-14}, 2×10^{-13}, 6×10^{-13}, 2×10^{-12} yr^{-1} pc^{-3} – left to right. Upper row of panels shows density and velocity fields at $t = 10$ Myr, lower row of panels is for $t = 30$ Myr.

our simulations, the heating rate is assumed to be time-independent and exponentially decreasing in the vertical direction with the scale height of the ISM disc. Such an assumption is sufficient to stabilize radiative cooling of ambient gas at $T = 9 \times 10^3$ K. Any deviation of the heating rate in the unperturbed gas violates the balance between cooling and heating and stimulates thermal instability, and leads to redistribution of gas mass in the interstellar disc (see e.g. in de Avillez 2000; Hill et al. 2012). In order to avoid contaminations of such effects we follow Li et al. (2017a) to assume the heating rate exponentially decreasing upwards across the entire computational domain.

Recently Fielding et al. (2017) studied the dynamics of an outflow generated by individual SNe spread throughout the galactic disc in relatively small galaxies with radial scale of $R_\mathrm{d} \sim 300$ pc. It follows from their consideration that among other factors a non-planar (spherical or quasi-spherical) geometry of the gravitational field and the ISM disc seems to be an essential condition for launching a large scale galactic outflow. When higher mass (disc) galaxies are concerned it is clear that certain conditions have to be fulfilled in order that the energy source – SN explosions in our case, would be able to expel gas at heights where non-planar effects come into play. It occurs normally at scale heights comparable to the disc radial scale (Kalberla 2003). However, our paper aims at a different aspect of the problem — how SNe can throw gas to small length scales (a few gas scale heights), corresponding to low to intermediate size gaseous haloes, observed in Milky Way size edge-on galaxies (Dahlem et al. 1995, 2000; Heesen et al. 2018), where the effects of diverging quasi-spherical geometry are weaker than in dwarf galaxies.

3 RESULTS

The ability of a single SN to break through the ISM layer and eject matter and energy out of the disc into the extra-planar space is determined by interrelation between the explosion energy E, the gas scale height z_0, and the in-plane density ρ_0. It can be loosely written as $\rho_0 z_0^3 \lesssim \eta_\mathrm{h} E c_\mathrm{s}^{-2}$, where $\eta_\mathrm{h} \sim 0.1$–0.3 is the heating efficiency – the fraction of energy left after radiative cooling, c_s, is the sound speed in ambient gas (see e.g. discussion in Ferrara & Tolstoy 2000). For typical parameter values it can be reduced to $nT_4 < 0.2\eta_\mathrm{h} z_{100}^{-3}$, which cannot be fulfilled for the ISM pressure $p \sim 3000$–10^4 K cm^{-3} and for $z_0 > 50$ pc. For an SN placed at a height z above the galactic plane this condition softens approximately by factor of e^{-z/z_0}, such that even a single SN explosion can break through the disc and eject mass and energy out of it. Then this means that if the scale height of SNe $z_\mathrm{sn} \gtrsim z_0$, even a relatively weak SF is able to heat halo and supply into it gas from exploding SNe and partly from the ISM disc as well. It is important to note, that even though the fraction of such outstanding SNe seems to lie in the range of Poisson noise, the two circumstances amplify their contribution: one is because of the above-mentioned weakened condition for breaking through the disc, the other is that for an SN exploding at $z \gtrsim z_0$ the remnant expands upwards faster than for those exploding in the plane. This circumstance can come into play in conditions with low SF and SN rates, when deviations from an average behaviour may be as considerable as $\propto \nu^{-1/2}$.

Fig. 2 (left column of panels) shows slices representing density distribution in the computational zone at times $t = 10$ Myr and $t = 30$ Myr for different SN rates in the disc with gas surface density $\Sigma_\mathrm{g} = 3.6\ \mathrm{M}_\odot\ \mathrm{pc}^{-2}$: 2×10^{-14}, 6×10^{-14}, 2×10^{-13}, 6×10^{-13}, 2×10^{-12} yr^{-1} pc^{-3} (the corresponding SF surface density rates range within $\Sigma_\mathrm{SF} \simeq (6 \times 10^{-4}$–$0.06)\ M_\odot\ \mathrm{yr}^{-1}\ \mathrm{kpc}^{-2}$, assuming the SN rate per mass $\nu_m \simeq (150\ \mathrm{M}_\odot)^{-1}$). The porosity factor $q = 2\pi R_0^2 z_0 \nu t_0 \sim z_{0,100}\nu_{-13} n^{-1}$ increases from ∼0.2 on the left to ∼2 on the right; here $t_0 = 3t_\mathrm{r} \sim n^{-1/3}$ Myr with t_r being the characteristic time when an expanding remnant enters the radiative phase, R_0, the remnant radius at $t = t_0$, $z_{0,100} = z_0/100$ pc, $\nu_{-13} = \nu/10^{-13}$ in

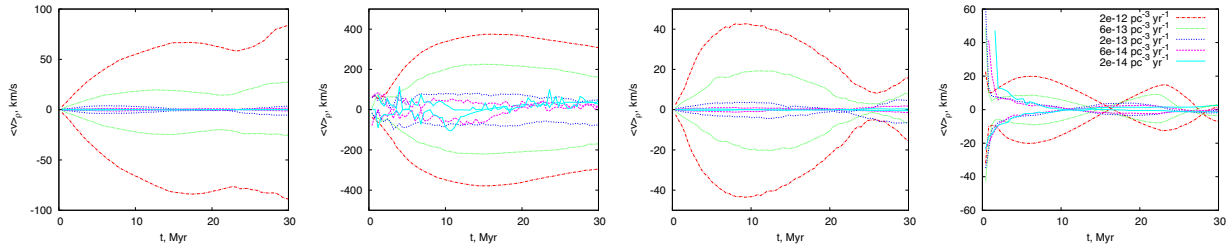

Figure 3. Mass-average velocity as a function of time for the models shown in Fig. 2: colours code SN rate from the lowest (cyan) to the higher (red) as shown in the legend; left-to-right panels show the mass-average velocity for the entire temperature range (left), for hot phases with $T > 10^5$ K (second), for the warm phases with temperature 10^3 K $< T \leq 10^5$ K (third), and for the cold phases with temperature $T \leq 10^3$ K (right); quasi-periodical variations of velocity for low-temperature phase reflects nearly ballistic free-fall motions of dense clouds with the characteristic time $t_{\rm ff} \simeq 15$ Myr for clouds within $|z| \lesssim 300$ pc in model with the highest SN rate.

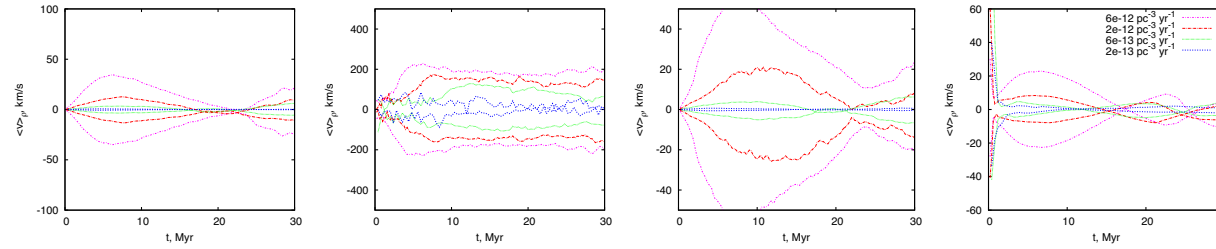

Figure 4. Mass-average velocity as a function of time for the same thermal phases as in Fig. 3 in the models with $\Sigma_{\rm g} = 10.8$ M$_\odot$ pc^{-2} (the mid-plane density $n = 3$ cm^{-3}). Line colours correspond to the same SN rate as in Fig. 3 except magenta line, which depicts the dependence for SN rate 6×10^{-12} yr^{-1} pc^{-3}.

units yr^{-1} pc^{-3}. Factor q characterizes the fraction of overlapped remnants from individual SNe – in the left side overlapping is small and remnants from individual SNe remain isolated without the production of a collective effect. It is clearly seen that for galactic discs with stellar scale height $z_* = 100 z_{*,100}$ pc models with the surface SFR smaller than $\Sigma_{\rm SF} < 0.006\ z_{*,100}M_\odot$ yr^{-1} kpc^{-2} (SN rate $\nu < 2 \times 10^{-13}$ yr^{-1} pc^{-3}) for which $q < 1$ may show strong deviations from symmetry between hydrodynamic fields above and below the plane – reminiscent of spontaneous symmetry breaking.

In general, the outflow weakens with time because a fraction of gas cools and condenses into colder and denser clouds and cloudlets under compression from overlapping shocks. When sufficient time has elapsed most massive of them turn to fall down even though SN rate stay constant. Clouds start forming along the outflow due to thermal instability enhanced by shock compression at times $t \sim 0.1$–0.3 Myr. They are seen on the density field in Fig. 2 as small dense clumps. Once clouds are formed the interrelation between pressure and gravity forces acting on them changes: the dominant forces on the are ram pressure from hot diffuse ambient gas $\propto R_{\rm cl}^2$ and gravitational force $\propto R_{\rm cl}$, $R_{\rm cl}$ being cloud radius. This circumstance results in a gradual decrease of the mass-averaged gas velocity between $t \simeq 15$ and $t \simeq 25$ Myr as shown in Fig. 3 (first panel). It is also seen if one compares the velocity fields at $t = 10$ Myr and $t = 30$ Myr in Fig. 2. Models with smaller SN rate do not form a developed gas circulation, but rather a sporadic isolated growing or contracting bubbles without such a pronounced collective effect as seen in case of high SN rate. It is a consequence of the fact that the porosity factor for these models is small and there is no percolation of different remnants. In models with high SN rate the mass-averaged velocity is regulated by hot gas phase before $t \lesssim 20$ Myr, even though its small mass (second panel). Quasi-periodic oscillations are clearly seen for the cold phase (right-hand panel). It reflects nearly ballistic motions of dense clouds within $|z| \lesssim 300$ pc with the characteristic free-fall time $t_{\rm ff} \simeq 15$ Myr for the highest SN rate and decreasing to $t_{\rm ff} \simeq 10$ Myr in for the lowest SN rate. Warm phases also seem to show quasi-periodic motions with longer characteristic times mediated by pressure (third panel). A small increase of the mass-average velocity for all phases (left-hand panel) is due to such a quasi-periodic increase in the velocity of warm phases (third panel) at $t \sim 30$ Myr.

In order to understand how the overall picture depends on gas distribution we have carried out several runs for higher gas surface density equal to $\Sigma_{\rm g} = 10.8$ M$_\odot$ pc^{-2}. Due to faster radiative cooling in denser environment one can expect more abundant formation of dense clouds and less efficient mass outflow to higher heights. It is indeed seen in mass-average outflow velocities (Fig. 4) with the magnitude smaller by factor 2. At the same time, one notes a similarity between the mass-average velocities in a diffuse and denser medium: comparing the velocities of warm and cold phases in Figs 3 and 4 one can see that a three times higher SN rate (magenta lines in Fig. 4) in a three times denser gas produces mass-average outflows which are close (within ∼20 per cent) to those in less dense gas with proportionally lower SN rate. Therefore, the ratio $\nu_{\rm SN}/n$ may represent sort of a scaling factor describing dependence of warm and cold outflows on SF and density environment.

In order to illustrate details of the initial (within $t \sim 1$ Myr) development of outflows in the low and high SN rates we show in Fig. 5 the 'velocity–density' distributions for 2×10^{-14} (left-hand panels) and 2×10^{-12} yr^{-1} pc^{-3} (right-hand panels) SN rates. It illustrates that such a transition from the outflow in the early episodes towards circulation of gas and subsequent settling down occurs within the initial 1.5 Myr: SN shock waves accelerate diffuse gas, compress it and when the shock fronts decelerate below $v_{\rm s} \lesssim 100$ km s^{-1} they cool radiatively and form denser clumps via thermal instability. Further fragmentation under thermal instability and formation of clumps occurs in this velocity range with

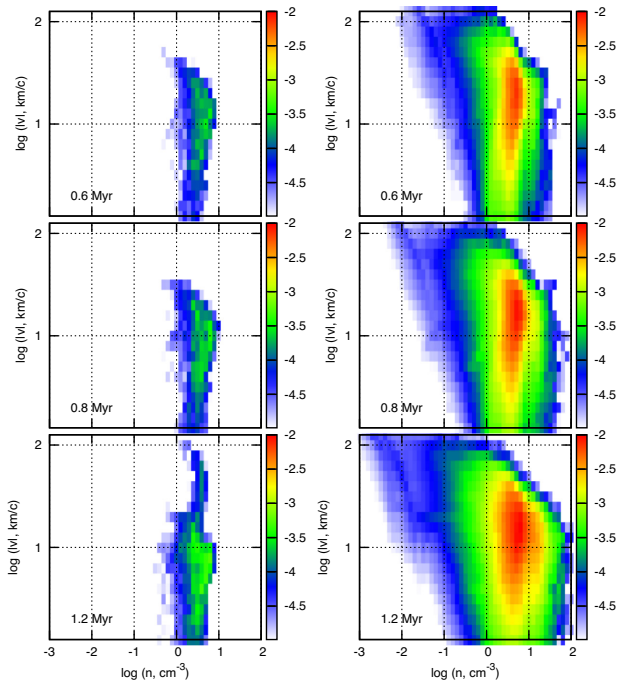

Figure 5. Velocity versus density within the initial ∼1 Myr episode of SN activity for the model with $\nu = 2 \times 10^{-14}$ yr^{-1} pc^{-3} (left) and $\nu = 2 \times 10^{-12}$ yr^{-1} pc^{-3} (right); times are 0.6, 0.8, 1.2 Myr from top to bottom. Colour coding corresponds to the mass fraction of gas in a given range of n and $|v|$. It is seen that after 0.6–0.8 Myr, gas accumulates in relatively dense 0.3 cm^{-3} $< n <$ 10^2 cm^{-3} clumps.

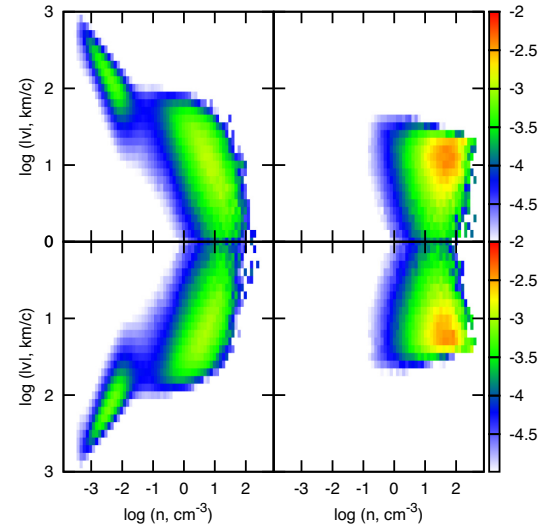

Figure 6. Contribution of outflowing – *left-hand panel*, and infalling – *right-hand panel*, gas into the 'velocity–density' diagram; upper panels are for gas above, and lower panels for gas below the plane for SN rate $\nu = 2 \times 10^{-12}$ yr^{-1} pc^{-3}, at time $t = 20$ Myr. Colour coding is as in Fig. 5. It seems worth mentioning that denser gas falling on the galactic plane has velocities corresponding to the intermediate-velocity clouds in the Milky Way galaxy (Wakker 2001).

subsequent slowing of clumps due to gravity and ram pressure. In Fig. 5 it manifests in a gradual growth of mass of a relatively dense (0.3 cm^{-3} $< n <$ 10^2 cm^{-3}) and low-velocity ($|v| \lesssim 70$ km s^{-1}) gas after $t = 0.6$–0.8 Myr – the distribution function in Fig. 5 widens from the high-density edge $n \simeq 20$ cm^{-3} at $t = 0.6$ Myr to the high-density edge $n \simeq 50$ cm^{-3} at $t = 0.8$ Myr. Only hot low-density gas continues flowing out. The amount of such gas at lower SN rates is negligible, and it remains such in further development as can be judged from Fig. 2.

A small fraction of hot low density gas penetrates between the denser clumps and expand with higher velocities $v > 70$ km s^{-1} upwards, while denser gas confined in clumps and clouds decelerates below $v < 70$ km s^{-1} and eventually falls on to the disc at $t > 10$ Myr under gravitational force. It is clearly seen in Fig. 6, where a similar interrelation between the velocities and densities as in Fig. 5 are shown separately for positive and negative z and outflowing and infalling velocities for the model with $\nu = 2 \times 10^{-12}$ yr^{-1} pc^{-3} at the time 20 Myr. In the left-hand panel Fig. 6 (v, n)-plane is shown for outflowing gas – i.e. gas moving upwards with the upper and lower sub-panels showing $z > 0$ and $z < 0$ parts of the gaseous disc. The right-side panel shows interrelation between the velocities and densities of the gas moving downwards, i.e. corresponding to the inflow, and again the upper and lower parts of this panel show positive and negative z of the disc. In other words, the contributions of outflowing and infalling gas into the 'velocity–density' diagram separately for outflowing and infalling gas above and below the galactic plane at time 20 Myr are shown. It is seen that the dominant contribution to the domain of dense gas with velocities $|v| < 100$ km s^{-1} on both sides of the ISM disc comes from gas falling back on to plane. They look very symmetric and it exactly corresponds to quasi-periodic variations of the mass-average velocity for the cold $T < 10^3$ K phase in Fig. 3.

At longer time-scales gaseous discs with low SF and SN rates – lower than $\Sigma_{\rm SF} < 0.006\, z_{*,100}\, {\rm M}_\odot$ yr^{-1} kpc^{-2} and $\nu < 2 \times 10^{-13}$ yr^{-1} pc^{-3}, correspondingly, slightly puff out and remain apparently confined within the same scale height (see discussion below).

Therefore, this process – gas clumping due to fragmentation, results in the decrease of mass outflow rate on longer times $t \simeq$ 15–20 Myr, even when SN explosions are active. Fig. 7 displays the dependence of gas mass fractions $f_m(z)$, $f_{m,h}$ and $f_{m,c}$ deposited at a given height z on time for the models shown in Fig. 2. The upper row shows the fraction of gas in the entire temperature range, the second from top row shows fraction of hot ($T > 10^5$ K) gas, the third – fraction of warm $10^3 < T < 10^5$ K gas, while the lower – fraction of low-temperature ($T < 10^3$ K) phase. By definition $\int_{-\infty}^{\infty} f_{\rm m}(z)\,{\rm d}z = 1$, $\int_{-\infty}^{\infty} f_{\rm m,h}(z)\,{\rm d}z = \mu_{\rm h}$, $\int_{-\infty}^{\infty} f_{\rm m,w}(z)\,{\rm d}z = \mu_{\rm w}$, $\int_{-\infty}^{\infty} f_{\rm m,c}(z)\,{\rm d}z = \mu_{\rm c}$, and $\mu_{\rm h} + \mu_{\rm w} + \mu_{\rm c} = 1$. It is readily seen that most of the gas mass elevates during around 10–25 Myr depending on SN rate, and then reverses to fall on to disc regardless of continuous SN explosions. At the same time warm and hot gas continues to be elevated at longer times $t > 30$ Myr. This conclusion looks consistent with observations of extended hot (X-ray) haloes around edge-on galaxies with a relatively modest SFR. For instance, observations on *XMM–Newton* and *Chandra* of an edge-on galaxy NGC 891 reveal presence of hot ($T \sim 0.3$ keV) gas extending up to $z \sim 10$ kpc, which is comparable to the galaxy radius (Hodges-Kluck, Bregman & Li 2018).

An important feature seen in Fig. 7 is worth noting: models with low SN and SF rates ($\nu \leq 2 \times 10^{-13}$ yr^{-1} pc^{-3} and $\Sigma_{\rm SF} \simeq 6 \times 10^{-3} z_{*,100}\, {\rm M}_\odot$ yr^{-1} kpc^{-2}) reveal a very weak elevation of gas at heights $z < 300$ pc. It corresponds to a 'puffing out' of circulations at low height mentioned above, and the value $\nu \leq 2 \times 10^{-13}$ yr^{-1} pc^{-3} equivalent to the surface energy input rate $\leq 1.4 \times 10^{-4} z_{*,100}$ erg s^{-1} cm^{-2}; here the surface SN rate has been

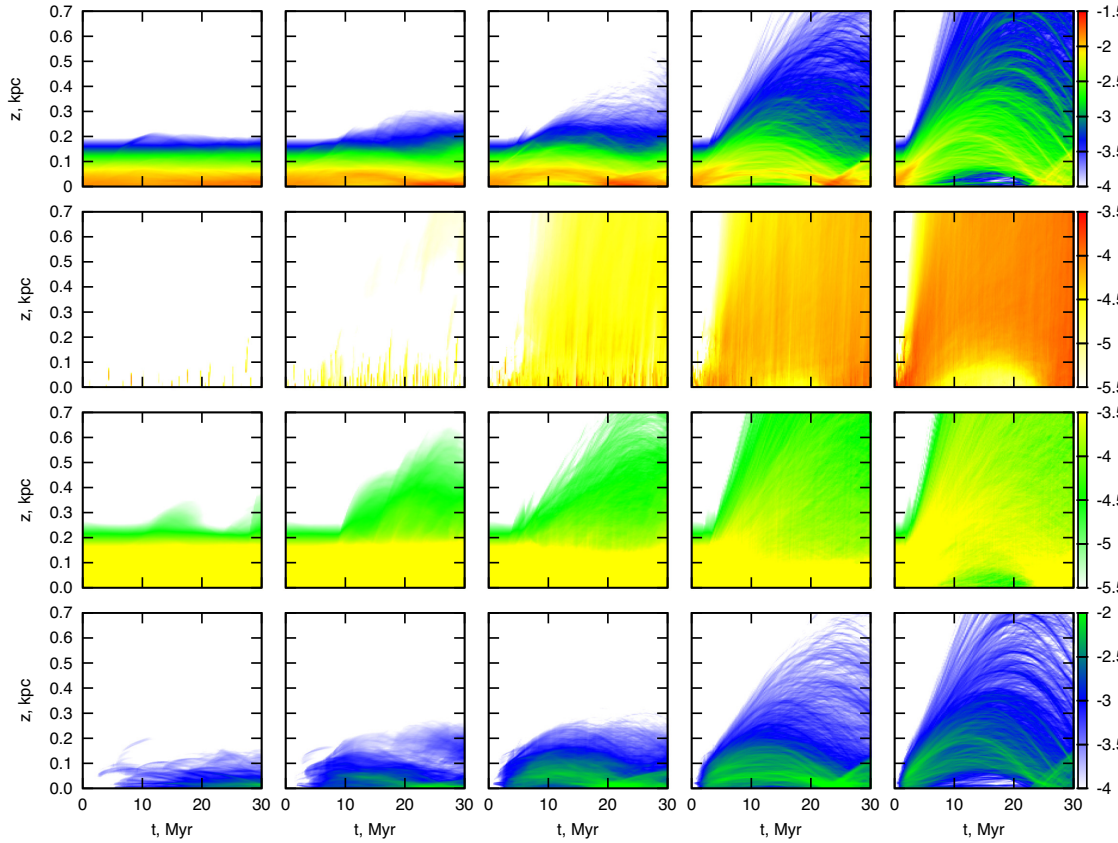

Figure 7. Fraction of gas mass at a given height z versus time for the models depicted in Fig. 2. *Top to bottom*: all gas, hot – $T \geq 10^5$ K, warm – $10^3 < T < 10^5$ K, and cold – $T \leq 10^3$ K components. Colour bars in the right show the mass fraction accumulated in a given gas component.

defined as a product of the volumetric SN rate by two stellar scale heights $2z_*$, see equation (2). For $z_* = 300$ as stated in Section 2 the energy threshold is $\leq 4 \times 10^{-4}$ erg s^{-1} cm^{-2}. This value may be treated as the threshold energy input rate necessary for driving gas outflows in the regime with disc-wide SN explosions.

Following the discussion above one can argue that a vertical distribution of warm and cold phases, similar case to the one shown in Fig. 7, is expected in models with higher density $\Sigma_g = 10.8$ M$_\odot$ pc^{-2} and proportionally higher SN rate. Moreover, as these phases dominate in mass compared to the hotter phases the total mass also follows this similarity. The following circumstance is worth noting: at large heights $z \gtrsim 5z_0$ (∼0.5 kpc) gas density reaches already the floor density $n \sim 10^{-3}$ cm^{-3}. Since at such heights the hot phase contributes considerably it turns out that the mass flow rate is approximately the same in the two models: $M_{|z|>5z_0}(3\Sigma_g, 3\nu_{SN}) \simeq M_{|z|>3z_0}(\Sigma_g, \nu_{SN})$.

This effect is intimately connected to a long-standing problem of 'mass entrainment' into shock-driven outflow meaning that hot dilute gas is inefficient to accelerate cold dense clouds (see detailed discussion in Scannapieco & Brüggen 2015; Schneider & Robertson 2017; Zhang et al. 2017). It is connected with the fact that a high density contrast between dense clouds and dilute hot gas is typically $\chi > 100$, and characteristic acceleration time is much longer than the cloud crashing time. In order to overcome this problem Gronke & Oh (2018) recently suggested that an additional radiative cooling in a turbulent mixing layer stimulates enhancement of mass loading of the outflowing low density gas. However, for typical parameters of clouds and ambient gas it may take ∼30 Myr which is longer than local starburst events in discs.

So far we have considered the efficiency of mass transport from the disc in terms of mass-averaged velocity (Figs 3 and 4) and mass fraction that reaches a given height (Fig. 7). Another key quantity describing the mass transport is the mass loading factor: $\beta = \dot{M}_g/\dot{M}_{SF}$, with $\dot{M}_g$ being the mass outflow rate, and $\dot{M}_{SF}$ the SFR in the underlying disc (Veilleux et al. 2005; see also equation 9 in Kim & Ostriker 2018). Fig. 8 presents β for three models with the three highest SN rates depicted in Fig. 2: $\nu = 2 \times 10^{-13}$, 6×10^{-13}, 2×10^{-12} yr^{-1} pc^{-3} (from left to right) in the disc with $\Sigma_g = 3.6$ M$_\odot$ pc^{-2} for the three thermal phases (hot – $T \geq 10^5$ K, warm – $10^3 < T < 10^5$ K and cold – $T \leq 10^3$ K) and their sum. The fractional mass-loading factors demonstrate features seen above in mass-average velocities: the cold and warm phases show periodic variations connected with formation of cloudlets, falling back on to the plane and turning around after two free-fall times; the hot phase flows out continuously, although with intermittent vertical stripes caused by cooling and falling of cold fragments downwards; and the sum of fractional mass-loading factors. When integrated over time the fractional mass-loading factors demonstrate vertical behaviour close to the ones found on larger time and spatial scales by Kim & Ostriker (2018) (see their fig. 9): predominance of the cold phase at low heights, and the hot phase on large heights.

The overall behaviour of mass-loading factors is modelled to a certain extent by the mass-average velocities, including their de-

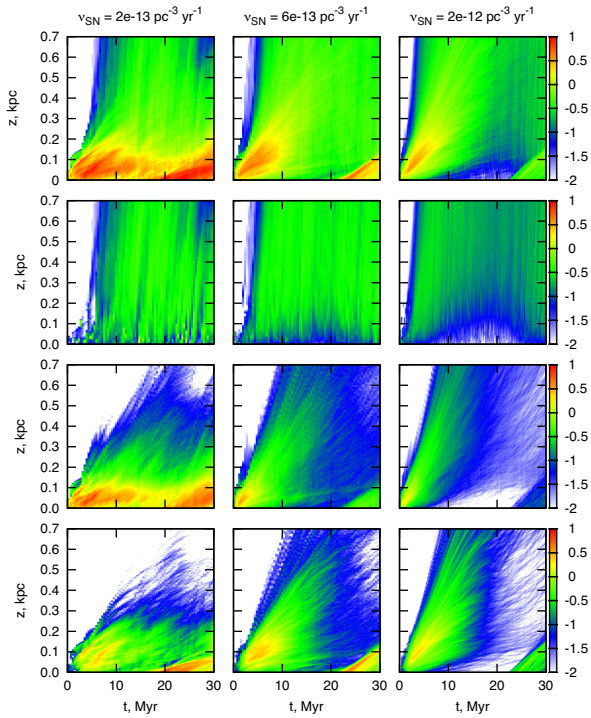

Figure 8. Mass-loading factor, $\log\beta$, at a given height z versus time for SN rate 2×10^{-13}, 6×10^{-13}, 2×10^{-12} yr^{-1} pc^{-3} (from left to right) in the disc with gas surface density $\Sigma_g = 3.6$ M$_\odot$ pc^{-2}, the corresponding density slices are depicted on three right panels in Fig. 2. *Top to bottom*: all gas, hot – $T \geq 10^5$ K, warm – $10^3 < T < 10^5$ K, and cold – $T \leq 10^3$ K components.

pendence on SN rates. One therefore can conclude that proportional increase of SN rates and surface densities will leave intact a general picture of time and spatial variations of mass-loading factors. More explicitly one can think that mass-loading factors in models with high density $\Sigma_g = 10.8$ M$_\odot$ pc^{-2} will be similar to what shown in Fig. 8 but for proportionally increased SN rates: 6×10^{-13}, 2×10^{-12}, 6×10^{-12} yr^{-1} pc^{-3}.

4 OBSERVATIONAL CONSEQUENCES

Hot low density gas inside expanding bubbles and outflows can be observed in emission and absorption in far-UV and X-ray ranges. Black points in Fig. 9 depict 'temperature–density' relations from available observational data compiled in Gupta et al. (2018, see their table 3). For comparison we show scatter plots connecting temperature and density through the whole computational zone for the models with 2×10^{-14}, 6×10^{-14}, 2×10^{-13}, 6×10^{-13}, 2×10^{-12} yr^{-1} pc^{-3} at several epochs. The two upper rows correspond to early times: 0.2 and 1.4 Myr, whereas the two lower correspond to the middle time, 10 Myr, and at the final epoch, 30 Myr. A noticeable trend is that only young dynamical states – $t \lesssim 1.5$ Myr of the ISM with a high SFR ($\nu \geq 2\times10^{-13}$ yr pc^{-3}) contain hot and relatively dense gas seen observationally. This may arise from the fact that the X-ray emission from dilute hot gas does not contribute much and therefore is missed in observations compiled in Gupta et al. (2018). On the other hand, it is a natural consequence of a fast cooling ($t \lesssim 3$ Myr) of X-ray gas with density in the range 0.03 cm^{-3} $< n <$ 0.3 cm^{-3} – at longer times gas temperature falls below the observational level even in the low density range $n \sim 10^{-2}$ cm^{-3} and at high-energy injection rate as seen in third and fourth panels in Fig. 9. It is also clear that lower SN rates produce less hot gas in the entire relevant density range – the characteristic time between two subsequent shock waves impinging a given gas element for $\nu \lesssim 2\times10^{-13}$ yr^{-1} pc^{-3} is longer than the cooling time $t \lesssim 0.3$ Myr.

Fig. 10 presents the X-ray surface brightness $\log(I_X$, keV cm^{-2} s^{-1} sr^{-1}) in the *ROSAT* bands 0.1−0.3 keV (upper row) and 1.6−8.3 keV (lower row), for the models depicted in Fig. 2 (from left to right) at 10 Myr. Here we assume that the observer looks along the z-direction, in order to determine the maps in xy-plane. Absorptions by the gas layer on the line of sight between the emitting gas and the observer is accounted with the cross-section given by Wilms et al. (2000). As the absorption decreases with energy approximately as $\sigma(E) \propto E^{-2.5}$, the high-energy *ROSAT* band map is insensitive to absorption. For SN rate $\nu \gtrsim 2\times10^{-13}n^{4/3}$ yr^{-1} pc^{-3} with n being mean ambient density, the surface brightness in the low-energy band at $t \gtrsim 10$ Myr remains greater than 10^{-2} keV cm^{-2} s^{-1} str^{-1} inside the simulated area. This means that such SN rate produces a rather smooth steady state X-ray field – the absorption does not significantly change the brightness distribution, it shows only a difference within factor of 2 on small scales. For lower rates though, the distribution of the surface X-ray brightness is patchy – only separate regions of the ISM disc emit in this band within one cooling time and then disappear, making the soft X-ray surface pattern intermittent in space and time. In the high-energy a steady state X-ray field can be supported by SN rate $\nu \gtrsim 6\times10^{-13}n^{4/3}$ yr^{-1} pc^{-3}.

Fig. 11 presents the distribution functions of X-ray surface brightness – the probability to achieve the brightness in a given range, in the *ROSAT* bands for the models with $\nu = 2\times10^{-13}$, 6×10^{-13}, 2×10^{-12} yr^{-1} pc^{-3} for which a steady state X-ray field remains at 10 Myr (see Fig. 10). One can see a shift of the distributions towards higher energy bands as predicted in (Vasiliev et al. 2017). For the low-energy range, 0.1–0.3 keV, distributions for various SN rates are similar with a single sharp peak. One may expect a sort of relation between the peak value of surface brightness and SN rate.

In order to check this assumption we follow the evolution of the peak value for three values of the SN rate able to keep a steady state X-ray field within the first few million years. In top panel of Fig. 12 one can observe that the magnitude of the peak brightness I_{mx} saturates with time for 0.1–0.3 keV band. The bottom panel of Fig. 12 shows the relation 'peak X-ray brightness – SN rate' for different bands, the ambient gas density $n = 1$ cm^{-3} is assumed; thin dotted lines $\log I_{mx} \simeq \log\nu_{SN} - (0.2 + 0.5k)$, where $k = 0$, 1, 2, 3 count the X-ray bands from the softest $E = 0.1$–0.3 keV to the hardest $E = 1.6$–8.3 keV approximate the data. Coloured vertical lines show the spread of the X-ray brightness peak during the evolution from 10 to 30 Myr; for different bands lines have different thickness and are shifted right by $\Delta\log\nu_{SN} = 0.01$. This allows us to independently estimate the SN rate from X-ray observations.

In order to obtain spectral features of galactic outflows widely distributed through over interstellar discs we calculate the dependence of emission measure in different temperature bins versus velocity along several lines of sight perpendicular to the disc. These values calculated in numerical cells within the velocity $[v, v + \Delta v]$ are believed to reflect both optical and X-ray emissivity of outflows (e.g. in lines of metal ions like C IV, O VI, O VII, Ne VIII, Ne IX, Mg X, etc.); the velocity ranges from −500 to +500 km s^{-1}. Such disc-wide outflows appear to be relatively quiescent as compared to violent explosive events in galaxies with a central starburst, as for instance, in M82 galaxy. Their spectral features are

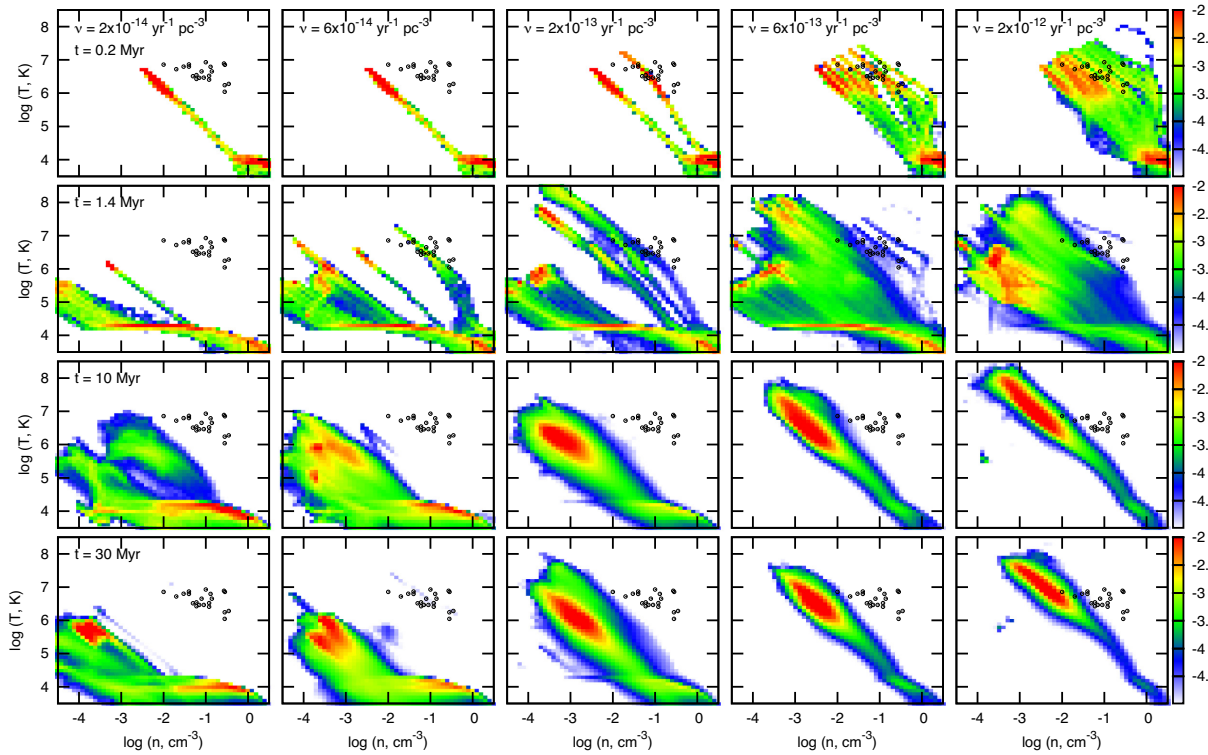

Figure 9. The temperature–density distribution for the models with $\nu = 2 \times 10^{-14}$, 6×10^{-14}, 2×10^{-13}, 6×10^{-13}, and 2×10^{-12} yr^{-1} pc^{-3} from left to right; time moments are 0.2, 1.4, 10, and 30 Myr from top to bottom. The black points depict the observational data for interstellar superbubbles taken from table 3 of Gupta et al. (2018).

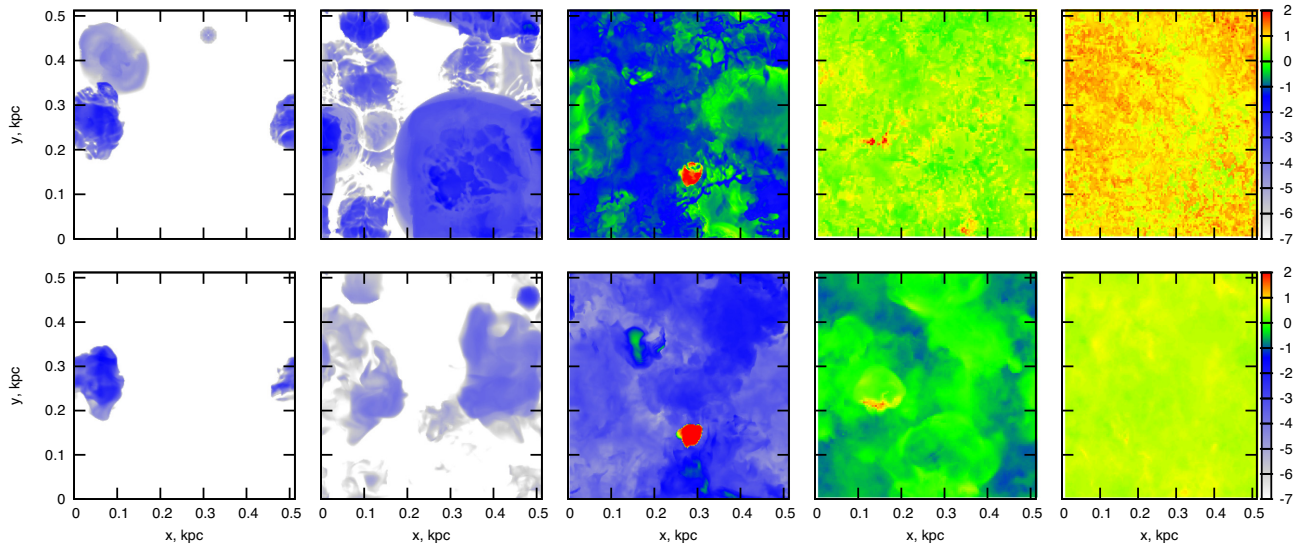

Figure 10. The X-ray surface brightness [log (I_X, keV cm^{-2} s^{-1} str^{-1})] maps in the *ROSAT* bands 0.1–0.3 keV (upper row) and 1.6−8.3 keV (lower row) for the models depicted in Fig. 2 (from left to right) at 10 Myr.

also less pronounced than in the case of strong winds from galactic centres.

Fig. 13 shows scatter plots for the emission measure along 300 lines of sight in z-direction in the model with $\nu = 6 \times 10^{-13}$ yr^{-1} pc^{-3} ($\Sigma_{SF} \simeq 0.02$ M$_\odot$ yr^{-1} kpc^{-2}, upper panel) and $\nu = 2 \times 10^{-12}$ yr^{-1} pc^{-3} ($\Sigma_{SF} \simeq 0.06$ M$_\odot$ yr^{-1} kpc^{-2}, lower panel) for $t = 30$ Myr. It is seen that the EM-velocity profiles reveal a distinct two-peak shape corresponding to outflowing gas at $v = \pm 100$ km s^{-1} for lower SN rate and at $v = \pm 200$ km s^{-1} for higher SN rate for the temperature bin $T = 10^6$–10^7 K, while the EM value at higher temperature bin $T \geq 10^7$ K shows the peaks at $v = \pm 250$ km s^{-1} for smaller SN rate and $v = \pm 400$ km s^{-1} for higher SN rate. Note that there is no two-peak velocity distribution for SN rate $\nu \lesssim 2 \times 10^{-13}$ yr^{-1} pc^{-3}, because

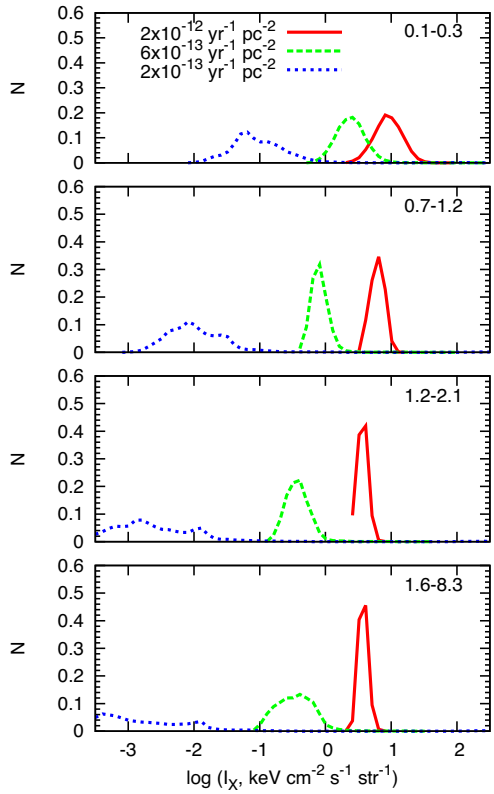

Figure 11. Distribution functions (histograms) of X-ray surface brightness in the *ROSAT* bands (0.1–0.3, 0.7–1.2, 1.2–2.1, 1.6–8.3 keV from top to bottom) for the models with 2×10^{-13} yr^{-1} pc^{-3} (blue), 6×10^{-13} (green), $\nu = 2 \times 10^{-12}$ (red); stable smooth X-ray fields with narrow distributions are kept at 10 Myr only for models with $\nu > 2 \times 10^{-13}$ yr^{-1} pc^{-3}, for lower SN rates the distributions are wide and nearly flat (see Fig. 10).

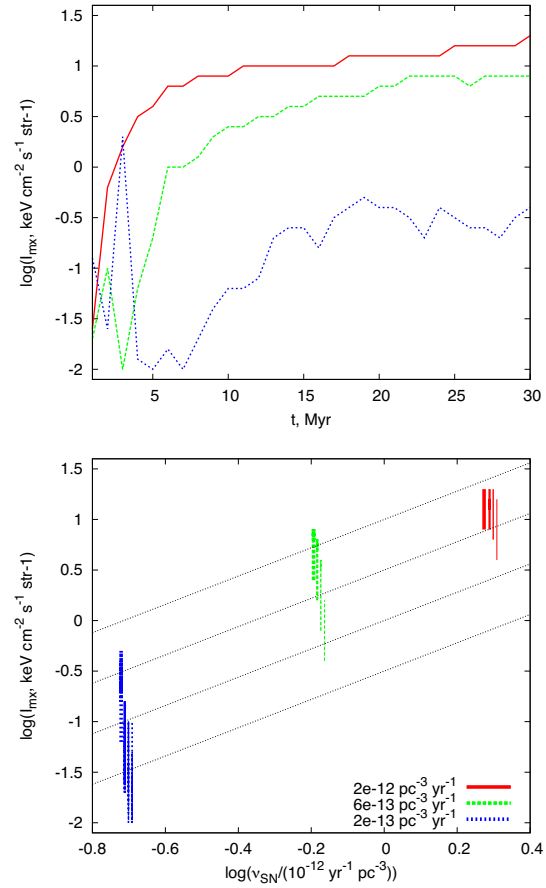

Figure 12. *Top panel.* The evolution of the peak value of X-ray surface brightness as shown in the distribution function for 0.1–0.3 keV band on upper panel of Fig. 10. *Bottom panel.* The dependence 'peak of X-ray brightness – SN rate'. The colour vertical lines correspond to the dispersal of the peak during the evolution from 10 to 30 Myr: from left to right they correspond to the bands 0.1–0.3, 0.7–1.2, 1.2–2.1, 1.6–8.3 keV, for the sake of clarity they have different thickness and shifted by $\Delta \log \nu_{\rm SN} = 0.01$. The dotted lines show linear functions $\log I_{\rm mx} \simeq 1.4 \log \nu_{\rm SN} - (0.2 + 0.5k)$, the value of k changes from soft to hard bands.

there is no outflow signature for such SN rate. In this case the velocity distribution has one peak around zero with dispersion lower than 50 km s^{-1}. Therefore measurements of such profiles can provide an estimate of hot gas density and the corresponding mass outflow rate. It is worth noting that the peak velocities are factor of $\sqrt{A}$ higher than the thermal Doppler line width, where A is atomic number of the ion, and thus macroscopic outflow motion seems to be easily recognizable. Moreover, an additional feature for discrimination of thermal line broadening and its shift due to macroscopic motion is the non-Gaussian line profile for the latter case.

5 CONCLUSIONS

We have studied how isolated SN remnants spread through over the disc merge into collective bubbles depending on the SN rate and eject interstellar gas into haloes. Our results are summarized as follows:

(i) In the initial episodes of SN activity during $\sim$1 Myr gas cools radiatively, fragments and forms dense clumps. On next stages two flows do form: high-velocity ($|v| \geq 70$ km s^{-1}) hot diffuse gas along with low-velocity ($|v| \leq 70$ km s^{-1}) dense gas moving outwards, and counter flowing low-velocity ($|v| \leq 70$ km s^{-1}) dense clumps moving inwards. This conclusion is consistent with estimates inferred from numerical simulations by Kim & Ostriker (2018) within the vertical scales of our models, though the mass-loading factor – the ratio of mass outflow rate to the SFR, for hot gas is an order of magnitude lower $\sim 0.01 n z_{100}$. The mass-loading factor for cold phase ($T < 10^3$ K) sharply decreases after a free-fall time when dense clumps start moving downwards.

(ii) With changing of gas density $\Sigma_{\rm g}$ and SN rate ν the vertical structure of gas outflow and its characteristics remains nearly invariant if ν and $\Sigma_{\rm g}$ change proportionally: $\nu/\Sigma_{\rm g} = {\rm const}$.

(iii) Within the regime of disc-wide SN explosions the threshold energy input rate for driving hot gas outflows can be estimated as $\sim 4 \times 10^{-4}$ erg s^{-1} cm^{-2} for stellar scale height $z_* = 300$ pc.

(iv) After $t \gtrsim 10$ Myr outward motion weakens under gravity and eventually only a small fraction $\sim 3 \times 10^{-3}$ of cold gas remains at heights $\gtrsim 0.5$ kpc even for the rates $\sim 2 \times 10^{-12}$ yr^{-1} pc^{-3}. Hot and warm gas stay at heights $\sim$1 kpc on a longer time-scale >30 Myr. This results is consistent with observations of X-ray coronae around edge-on galaxies with a modest SFR $\nu \sim 2 \times 10^{-13}$ yr^{-1} pc^{-3}. For lower SN rates $\nu < 2 \times 10^{-14}$ yr^{-1} pc^{-3} its mass fraction falls though below $\sim 10^{-5}$.

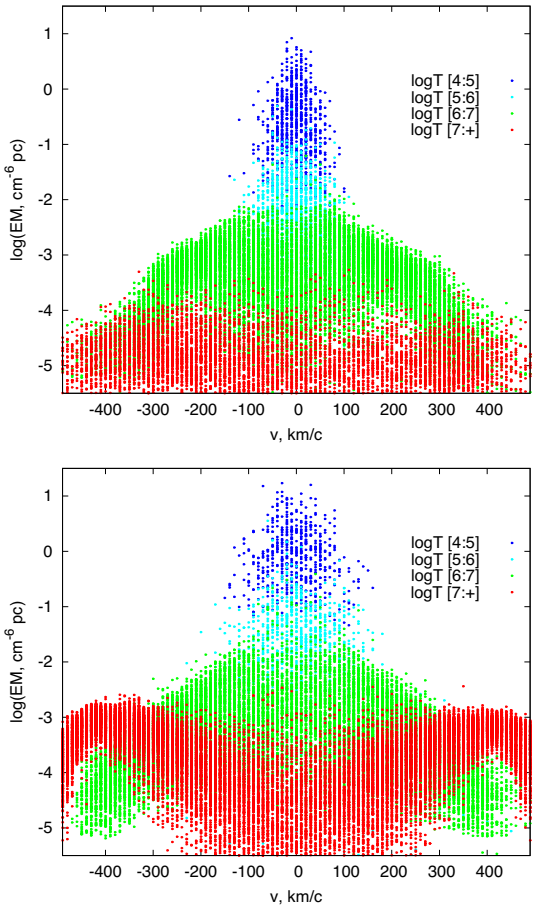

Figure 13. Dependence of emission measure versus velocity along the sightline perpendicular to the disc for different temperature bins as shown in colour legends; upper panel for SN rate $\nu = 6 \times 10^{-13}$ yr^{-1} pc^{-3}, lower panel for $\nu = 2 \times 10^{-12}$ yr^{-1} pc^{-3}.

(v) The interrelation between temperature and density in gas confined in bubbles nearly corresponds to an isobaric condition (though with a high spread). Observational X-ray data (as compiled in Gupta et al. 2018) likely correspond to young gas ($t \lesssim 1.5$ Myr) excited by SN explosions with a relatively high rate $\nu \gtrsim 2 \times 10^{-13}$ yr^{-1} pc^{-3}.

(vi) When seen face-on interstellar discs reveal either steady state or intermittent in space and time distribution of surface brightness through over the disc. High SN rate models with $\nu \gtrsim 2 \times 10^{-13}$ yr^{-1} pc^{-3} show one-peak brightness distribution function $F(I_X)$ in different energy bands with the peak brightness nearly linearly growing with SN rate.

(vii) Emission line profiles of highly ionized ions present in hot ($T \geq 10^6$ K) outflowing gas can serve as tracers of the outflow and allows to estimate hot gas density and the outflow mass rate.

ACKNOWLEDGEMENTS

YS thanks V. Dwarkadas for discussion. EV is grateful to the Ministry for Education and Science of the Russian Federation (grant 3.858.2017/4.6). The simulations have been supported by the Russian Scientific Foundation (grant 14-50-00043). YS is partially supported by the RFBR (grant 17-52-45053), by the project 01-2018 'New Scientific Groups LPI', and by the Program of the Presidium of RAS (project code 28). YS acknowledges support from Raman Research Institute where this work has been partly conducted.

REFERENCES

Bakes E. L. O., Tielens A. G. G. M., 1994, ApJ, 427, 822
Bigiel F., Leroy A., Walter F., Brinks E., de Blok W. J. G., Madore B., Thornley M. D., 2008, AJ, 136, 2846
Chevalier R. A., Clegg A. W., 1985, Nature, 317, 44
Dahlem M., Liesenfeld U., Golla G., 1995, ApJ, 444, 119
Dahlem M., Liesenfeld U., Rossa J., 2006, A&A, 457, 121
de Avillez M. A., 2000, MNRAS, 315, 479
Ferrara A., Tolstoy E., 2000, MNRAS, 313, 291
Fielding D., Quataert E., Martizzi D., Faucher-Gugiéra C.-A., 2017, MNRAS, 470, L39
Fielding D., Quataert E., Martizzi D., 2018, MNRAS, 481, 3325
Frisch P., Dwarkadas V., 2018, in Alsabti A. W., Murdin P., eds, Handbook of Supernovae. Springer, Cham
Gatto A. et al., 2017, MNRAS, 466, 1903
Gilmore G., Reid N., 1983, MNRAS, 202, 1025
Girichidis P., Walch S., Naab T., 2016, MNRAS, 456, 3432
Gronke M., Oh S. P., 2018, MNRAS, 480, L111
Gupta S., Nath B. B., Sharma P., Eichler D., 2018, MNRAS, 473, 1537
Hakobyan A. A. et al., 2017, MNRAS, 471, 1390
Heckman T. M., 2002, in Mulchaey J. S., Stocke J., eds, ASP Conf. Ser. Vol. 254, Extragalactic Gas at Low Redshift. Astron. Soc. Pac., San Francisco, p. 292
Heckman T. M., 2003, Rev. Mex. Astron. Astrofis. Ser. Conf., 17, 47
Heesen V. et al., 2018, MNRAS, 476, 158
Hill A. S., Joung M. R., Mac Low M.-M., Benjamin R. A., Haffner L. M., Klingenberg C., Waagan K., 2012, ApJ, 750, 104
Hodges-Kluck E. J., Bregman J. N., Li J.-T., 2018, ApJ, 866, 126
Kalberla P. M. W., 2003, ApJ, 588, 805
Kalberla P. M. W., Kerp J., 2009, ARA&A, 47, 27
Kennicutt R. C. Jr, 1998, ApJ, 498, 541
Kennicutt R. C., Evans N. J., 2012, ARA&A, 50, 531
Khoperskov S. A., Vasiliev E. O., 2017, MNRAS, 468, 920
Kim C.-G., Ostriker E. C., 2015, ApJ, 802, 99
Kim C.-G., Ostriker E. C., 2018, ApJ, 583, 173
Klingenberg Ch., Schmidt W., Waagan K., 2007, J. Comp. Phys., 227, 12
Krumholtz M. R., Dekel A., McKee C. F., 2012, ApJ, 745, 69
Lehnert M. D., Heckman T. M., 1996, ApJ, 472, 546
Li J.-T., Wang Q. D., 2013, MNRAS, 435, 3071
Li M., Bryan G. L., Ostriker J. P., 2017a, ApJ, 841, 101
Li M., Bryan G. L., Ostriker J. P., 2017b, ApJ, 831, L10
Mac-Low M.-M., Ferrara A., 1999, ApJ, 513, 142
Melso N., Bryan G. L., Li M., 2019, ApJ, 872, 47
Rossa J., Dettmar R.-J., Walterbos R. A. M., Norman C. A., 2004, AJ, 126, 674
Rubin K. H. R., Prochaska J. X., Koo D. C., Phillips A. C., Martin C. L., Winstrom L. O., 2014, ApJ, 794, 156
Scannapieco E., Brüggen M., 2015, ApJ, 805, 158
Schmidt M., 1959, ApJ, 129, 243
Schneider E. E., Robertson B. E., 2017, ApJ, 834, 144
Semenov V. A., Kravtsov A. V., Gnedin N. Y., 2018, ApJ, 861, 4
Sharma P., Roy A., Nath B. B., Shchekinov Yu., 2014, MNRAS, 443, 3463
Shchekinov Yu. A., 2018, Galaxies, 6, 62
Sofue Y., Wakamatsu K.-I., Malin D. F., 1994, AJ, 108, 2102
Suchkov A. A., Balsara D. S., Heckman T. M., Leitherer C., 1994, ApJ, 430, 511
Thompson T. A., Quataert E., Norman M., 2005, ApJ, 630, 167
Toro E., 1999, Riemann Solvers, Numerical Methods for Fluid Dynamics, 2nd edn. Springer-Verlag, Berlin
Tüllmann R., Breitschwerdt D., Rossa J., Pietsch W., Dettmar R.-J., 2006, A&A, 457, 779
Vasiliev E. O., 2011, MNRAS, 414, 3145

Vasiliev E. O., 2013, MNRAS, 431, 638
Vasiliev E. O., Nath B. B., Shchekinov Yu. A., 2015, MNRAS, 446, 1703
Vasiliev E. O., Nath B. B., Shchekinov Yu. A., 2017, MNRAS, 468, 2757
Veilleux S., Cecil G., Bland-Hawthorn J., 2005, ARA&A, 43, 769
Vijayan A., Sarkar K. C., Nath B. B., Sharma P., Shchekinov Yu., 2018, MNRAS, 475, 5513
Wakker B. P., 2001, ApJS, 136, 463
Walch S. et al., 2015, MNRAS, 454, 238
Wibking B. D., Thompson T. A., Krumholz M. R., 2018, MNRAS, 477, 4665
Wilms J., Allen A, McCray R., 2000, ApJ, 542, 914
Zhang D., Thompson T. A., Quataert E., Murray N., 2017, MNRAS, 486, 4801

This paper has been typeset from a TEX/LATEX file prepared by the author.